



OPEN

Synthesis and structural characterization of $\text{Ca}_{12}\text{Ga}_{14}\text{O}_{33}$

Sabrina E. A. McCoy^{1,2}, John R. Salasin², S. Michelle Everett³ & Claudia J. Rawn^{1,4}✉

$\text{Ca}_{12}\text{Ga}_{14}\text{O}_{33}$ was successfully synthesized using a wet chemistry technique to promote the homogenous mixing of the Ca and Ga cations. Rietveld refinements on X-ray and neutron powder diffraction data confirm that the compound is isostructural to $\text{Ca}_{12}\text{Al}_{14}\text{O}_{33}$, however, with a significantly larger lattice parameter allowing for the cages that result from the framework arrangement to expand. In naturally occurring $\text{Ca}_{12}\text{Al}_{14}\text{O}_{33}$, the mineral mayenite, these cages are occupied by O^{2-} anions, however, experimental studies exchanging the O^{2-} anions with other anions has led to a host of applications, depending on the caged anion. The functional nature of the structure, where framework distortions coupled with cage occupants, are correlated to electronic band structure and modifications to the framework could lead to interesting physical properties. The phase evolution was tracked using thermogravimetric analysis and high temperature X-ray diffraction and showed a lower formation temperature for the $\text{Ca}_{12}\text{Ga}_{14}\text{O}_{33}$ analogue compared to $\text{Ca}_{12}\text{Al}_{14}\text{O}_{33}$ synthesized using the same wet chemistry technique. Analyzing both X-ray and neutron powder diffraction using the Rietveld method with two different starting models results in one structural model, with one Ca position and the caged O on a $24d$ special position, being preferred.

The atomic structure of $\text{Ca}_{12}\text{Al}_{14}\text{O}_{33}$, also known as C12A7, consists of a positively charged cage-like framework where occluded anions occupy a fraction of the cages to balance the positively charged framework. The diffusion of anions from cage to cage allows the material high ion mobility and the potential for ion storage¹. This functionality leads to applications for $\text{Ca}_{12}\text{Al}_{14}\text{O}_{33}$ as a CO_2 absorber², a catalyst³, and as an inorganic electride⁴. The highly functional nature of the material raises questions about isostructural compounds and their potential properties. Framework distortion and cage occupancy are correlated to electronic band structure changes responsible for electrical insulator to conductor transition. Further modifications to the framework through alteration of cations and charge balancing anions in the structure should lead to changes in physical properties; the alteration of material properties with atomic substitutions has been experimentally and theoretically explored and are summarized in⁵. The ionic radius of Ga^{3+} in fourfold coordination with O is 47 pm compared to the 39 pm radius of Al^{3+} ⁶ suggesting that this substitution could result in a cage with a larger diameter. Partial site replacement of tri-valent Al cations has been performed with similar tri-valent Ga cations. However, results led to the conclusion that the single phase $(\text{Ca}_{12}\text{Al}_{14-x}\text{Ga}_x\text{O}_{32})\text{O}$ formed when $x = 1$ and when $x = 2$ both $\text{Ca}_5\text{Ga}_6\text{O}_{14}$ and $\text{Ca}_3\text{Al}_2\text{O}_6$ were observed in addition to $\text{Ca}_{12}\text{Al}_{12}\text{Ga}_2\text{O}_{33}$ ⁷. When $\text{Ca}_{12}\text{Al}_{13}\text{GaO}_{33}$ was subjected to reducing conditions at 1350 °C for 6 h, buried in graphite powder, the compound decomposed to $\text{Ca}_3\text{Al}_2\text{O}_6$ and $\text{Ca}_{12}\text{Al}_{14-x}\text{Ga}_x\text{O}_{33}$ ⁷. The cause of decomposition is not known, but $\text{Ca}_{12}\text{Al}_{14}\text{O}_{33}$ structure in general demonstrates complicated thermodynamic instability/stability trends under dry reducing conditions above 1100 °C^{8,9}. The influence of Ga on the cage structure and localized electron behavior could alter the physical properties including the mobility of occluded species, either atomic, molecular, or electrons, and the electrical conductivity.

The existence of $\text{Ca}_{12}\text{Ga}_{14}\text{O}_{33}$ has been theorized due to the similarity of the $\text{CaO}-\text{Al}_2\text{O}_3$ and $\text{CaO}-\text{Ga}_2\text{O}_3$ binary phase diagrams and existence of isostructural compounds from the two systems including $\text{Ca}_5\text{Ga}_6\text{O}_{14}$ and CaGa_4O_7 . Many versions of the $\text{CaO}-\text{Al}_2\text{O}_3$ binary phase diagram exist due to the importance of $\text{CaO}-\text{Al}_2\text{O}_3$ compounds to the cement industry. Using the Phase Diagrams for Ceramist online database 24 $\text{CaO}-\text{Al}_2\text{O}_3$ phase diagrams result with the earliest dating back to a 1955 dissertation¹⁰ followed by a 1956 version in the 2nd Edition of *The Chemistry of Cement and Concrete*¹¹. The latter shows the $\text{Ca}_{12}\text{Al}_{14}\text{O}_{33}$ compound and although some of the details have been refined the overall phase diagram remains generally unchanged. In 2001 Jerebstov and Mikhailov¹² published the $\text{CaO}-\text{Al}_2\text{O}_3$ diagram developed under anhydrous conditions and without moisture was not able to synthesis the $\text{Ca}_{12}\text{Al}_{14}\text{O}_{33}$ compound supporting an earlier observation by Nurse et al.¹³. In

¹Department of Materials Science and Engineering, University of Tennessee, Knoxville, USA. ²BWX Technologies, Lynchburg, VA, USA. ³Neutron Scattering Division, Oak Ridge National Laboratory, Oak Ridge, TN, USA. ⁴Center for Materials Processing, University of Tennessee, Knoxville, USA. ✉email: crawn@utk.edu

contrast when using the Phase Diagrams for Ceramist online database three CaO–Ga₂O₃ phase diagrams result. All three phase diagrams^{14–16} show the compounds Ca₃Ga₂O₆, CaGa₂O₄, and CaGa₄O₇ and the phase diagrams by Young¹⁵ and Kovba et al.¹⁶ show Ca₃Ga₄O₉ as a fourth intermediate compound. Conducting a database search of CaO–Ga₂O₃ compounds using the Inorganic Crystal Structure Database (ICSD)¹⁷ two other intermediate compounds, Ca₂Ga₂O₅¹⁸ and Ca₅Ga₆O₁₄^{19–21} have been reported, the former being synthesized with high-pressure. Londar²² grew Ca₅Ga₆O₁₄ crystals using the Czochralski method and starting with a 12CaO:7Ga₂O₃ mixture. Tolkacheva et al.²³ synthesized Ca₅Ga₆O₁₄ using solid state synthesis techniques and characterized the compound using X-ray diffraction, infrared and Raman spectroscopy, differential scanning calorimetry, thermogravimetric analysis, density measurements, and dilatometry. The latter was studied in both dry and moist atmospheres and after the sample was heated under moist conditions X-ray diffraction revealed CaGa₂O₄, Ga₂O₃, and CaCO₃, thought to have transformed from CaO during cooling in an environment where CO₂ was present.

It has previously been identified that the Ca₅Al₆O₁₄ phase forms through decomposition kinetics of Ca₁₂Al₁₄O₃₃, indicating that Ca₁₂Ga₁₄O₃₃ may be stable at low temperatures^{8, 24}. Similar to Ca₁₂Al₁₄O₃₃ it is expected the thermodynamic stability of the Ca₁₂Ga₁₄O₃₃ ($\rho = 3.54 \text{ g/cm}^3$) will be dependent on availability of anions that are able to stabilize cage structure over the layered and more dense CaGa₄O₇ ($\rho = 4.46 \text{ g/cm}^3$), Ca₃Ga₄O₉ ($\rho = 4.21 \text{ g/cm}^3$), and Ca₅Ga₆O₁₄ ($\rho = 4.12 \text{ g/cm}^3$) phases.

Here we report on the successful synthesis of Ca₁₂Ga₁₄O₃₃ through a solution-based route, provide a crystal structure characterization from X-ray and neutron powder diffraction data, evaluate the phase formation through thermogravimetric analysis (TGA) and high temperature X-ray diffraction (HTXRD) studies, and compare and contrast the Ca₁₂Al₁₄O₃₃ and Ca₁₂Ga₁₄O₃₃ compounds. Solution synthesis allows for homogenous mixing of the metal atoms, shortening diffusion pathways and allowing for kinetically favorable, but thermodynamically unfavorable, phases to form.

Experimental and methods

The polymer assisted sol–gel synthesis method was employed utilizing poly vinyl alcohol (PVA)²⁵. The 88% hydrolyzed PVA, with molecular weight between 20,000 and 30,000 g/mol, was dissolved in deionized water and allowed to stir for 1 h and Ca(NO₃)₂·4H₂O (ACS Grade, Fisher Chemical) and GaCl₃ (99.99 +%, Acros Organics) were dissolved separately into deionized water. The stoichiometry of the solutions was characterized through gravimetric titration. For synthesis, stoichiometric amounts of the Ca(NO₃)₂ and GaCl₃ solutions were added to the PVA solution and allowed to stir for 1 h prior to heating. A 4:1 ratio of the number of metal cations to PVA monomer units was used as previously identified as the ideal amount for Ca₁₂Al₁₄O₃₃⁸. The solution was heated on a 300 °C hotplate until most of solvent evaporated and the solution became viscous. The viscous liquid was placed in a 120 °C drying oven for 12 h and dried to a light foam; foaming occurs due to the evaporation of nitrate and chloride species. The foam was ground to a fine powder and divided for the various characterization studies.

Thermogravimetric Analysis (TGA) was performed on the dried non calcined polymer powder using a TA Instruments Q50 TGA. The sample was heated at a constant rate of 10 °C/min from 25 to 650 °C. Mass loss was recorded as a function of temperature.

A fraction of the powder was then calcined to 600 °C, based on the TGA data, to decompose the organics to allow for clean processing in the XRD environmental chamber, and immediately quenched. The resulting calcined powder was pressed into a 13 mm pellet. The remaining organic/inorganic PVA powder was retained for further thermal processing. Both room temperature and HTXRD data were collected using a Malvern PANalytical Empyrean diffractometer with a Cu radiation source operating with an accelerating voltage of 45 kV and current of 40 mA. A PIXcel^{3D} area detector with 255 active channels with $\sim 3^\circ 2\theta$ of coverage was used for rapid non-ambient data collection. For non-ambient data collection the sample was heated at 5 °C/min up to 800 °C, then the rate was slowed to 1.5 °C/min as the sample was heated to 1000 °C. Data were collected in the range from 25 to 36.5°2θ, this region contains major peaks related to the Ca₁₂Ga₁₄O₃₃ phase and possible secondary phases including Ga₂O₃, Ca₅Ga₆O₁₄, CaGa₂O₄, CaGa₄O₇, and Ca₃Ga₄O₉, and CaO. Using a 0.0131° step size and 13.77 s counting time each scan was approximately 1.5 min allowing for phase transitions to be detected while they occur. A longer data collection range, from 15–80°2θ, was used at 1000 °C to determine the full diffraction pattern and evaluate the evolved phases. The non-calcined powder was pressed into a pellet and was fired at 800 °C for 1 h. Subsequently ambient temperature data were collected from 15–120°2θ in high spatial resolution mode to verify the structure of the material and allow for refinement on the structural details including the lattice parameter, atomic positions, and atomic displacement parameters.

Time-of-flight powder neutron diffraction data were collected on the Nanoscale Ordered Materials Diffractometer (NOMAD) beamline²⁶ of the Spallation Neutron Source (SNS) at Oak Ridge National Laboratory (ORNL). About 1.5 g of near single-phase sample was contained in a 6 mm V sample canister. The partially calcined powder was fired at 800 °C for 1 h prior to loading the sample canister. NOMAD's detectors were calibrated using diamond, and silicon was used to generate the starting instrumental parameters. S(Q) was produced through normalizing the sample scattering via a solid vanadium rod and subtracting the background collected for an empty 6 mm V sample canister. Four individual data sets were collected and merged together for the data analysis.

HighScore Plus software package²⁷ interfaced with the ICDD PDF4 + database²⁸ was used for phase identification and the GSAS II software package²⁹ was used for the analyzing both the XRD and neutron diffraction data using the Rietveld method. For the data collected the lowest possible R obtainable for the data or wR_{min} , based in part on the number of data points and calculated in GSAS II, was 10.39% for the XRD data and 0.43% for the NPD data.

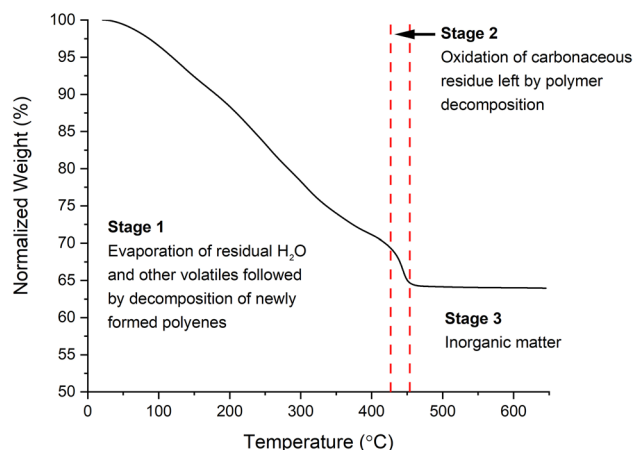


Figure 1. TGA showing the decomposition of the organics to inorganic matter from the unfired material.

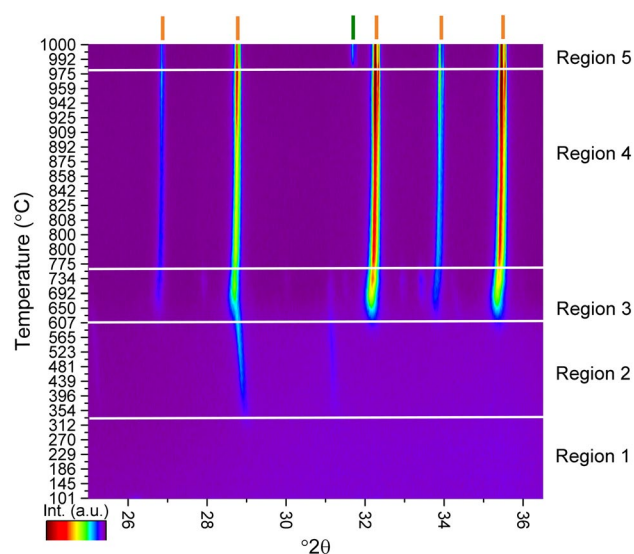


Figure 2. Intensity map of the HTXRD data from the pellet calcined at 600 °C. The orange dashes indicate the $\text{Ca}_{12}\text{Ga}_{14}\text{O}_{33}$ phase and the green dashes mark the CaO phase. Heatmap generated using the HighScore Plus software package²⁷, dash marks for indicating the CaO and $\text{Ca}_{12}\text{Ga}_{14}\text{O}_{33}$ phases determined from the ICSD¹⁷ and ICDD²⁸ databases.

Results and discussion

TGA characterization. Thermogravimetric analysis of the $\text{Ca}_{12}\text{Ga}_{14}\text{O}_{33}$ PVA powder, shown in Fig. 1, displays three decomposition stages during the heating. The first stage, from 25 °C to approximately 425 °C, shows the evaporation of residual H_2O and other volatiles remaining in the sample. When PVA is heated, polymer condensation reactions occur releasing structurally trapped water and causing polyenes to form and additional weight loss is due to the decomposition of the newly formed polyenes²⁵. In this region the decomposition follows a relatively constant slope, indicating that decomposition is uniform as the temperature increases. This is ideal for preventing segregation of species within the sample during calcination. The sharp drop in mass above 425 °C is likely caused by the oxidation of carbonaceous residue left by polymer decomposition²⁵. The sample experiences no further weight loss above 450 °C indicating that the remaining components in the sample are inorganic. The TGA results suggest that between 500 and 600 °C is the optimal temperature for calcination to ensure that all organics decompose. The sample experienced a total weight loss of 35% making this a high yield solution-based synthesis method.

XRD characterization. In-situ high temperature X-ray diffraction was used to observe phase transformations during heating in the data range from 25 to $36.5^\circ 2\theta$. The intensity heat map of the scans is shown in Fig. 2 and has five distinct phase regions. Representative patterns from each temperature region are shown in Fig. 3. Data collected on the 600 °C pre-calcined pellet shows that at temperatures below approximately 300 °C the

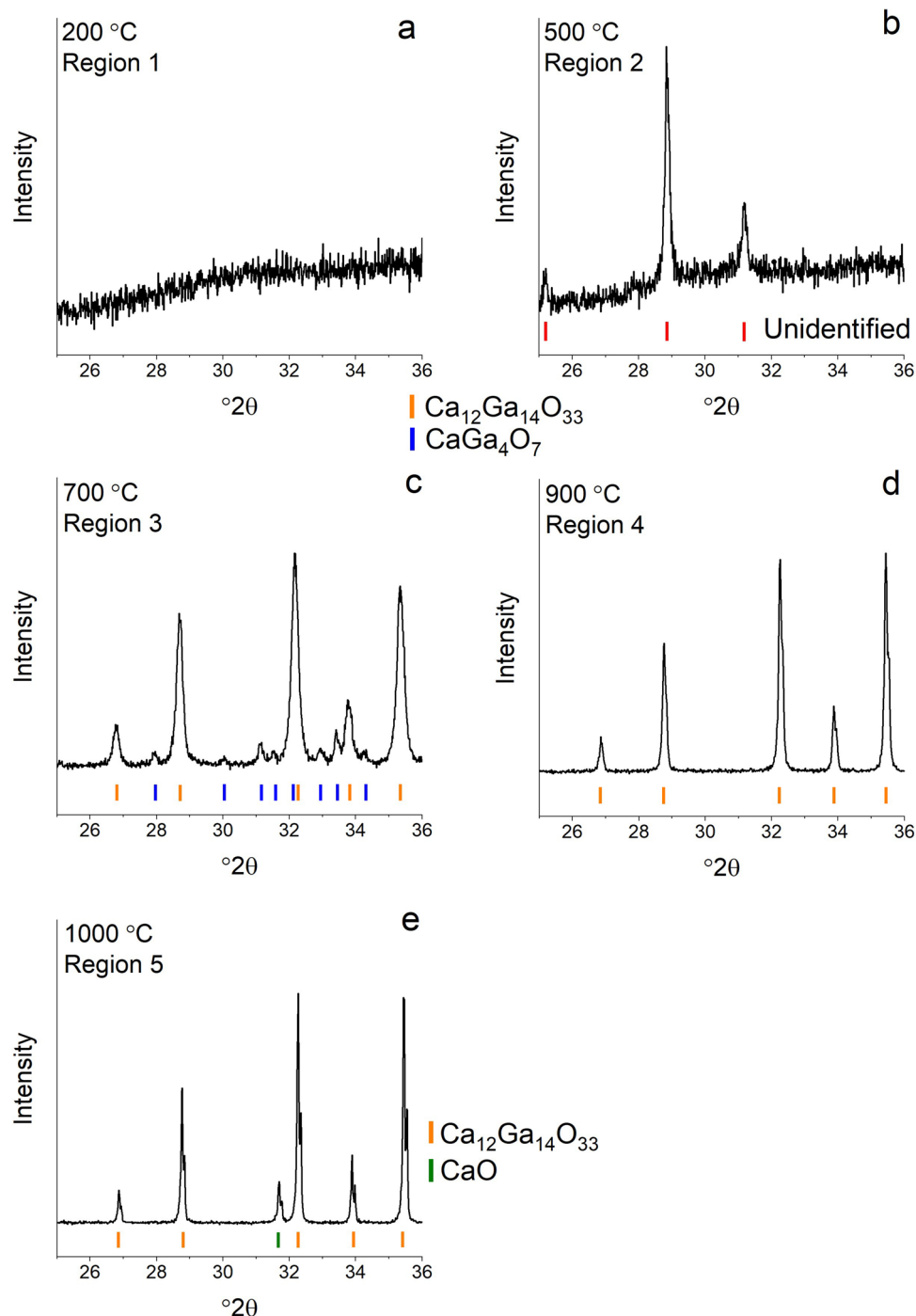


Figure 3. Representative X-ray powder diffraction data from selected temperature regions identified from the HTXRD results. Data collected at (a) 200 °C, (b) 500 °C, (c) 700 °C, (d) 900 °C, and (e) 1000 °C. Dash marks for indicating the CaO, CaGa_4O_7 , and $\text{Ca}_{12}\text{Ga}_{14}\text{O}_{33}$ phases determined from the ICSD¹⁷ and ICDD²⁸ databases.

sample is amorphous (Fig. 3a). After calcination most of the organics have been removed and a structureless mix of metal and oxygen atoms remains, with no diffraction peaks present in the data range. When heated above approximately 300 °C, two peaks appear at 28.9 and 31.2 2θ (Fig. 3b). In an attempt to identify the phase(s) that form between 300 and 650 °C data were collected in a larger 2θ range, between 10–80 2θ , and is shown in Fig. 4, revealing additional peaks associated with the phase(s). Despite attempts using the HighScore Plus software and the ICDD PDF4+ database, with and without chemical constraints, the peaks remain unidentified and could be representing either a single phase or a multiphase mixture. The sample had previously been heated to 600 °C during calcination to remove the organics, so this phase transformation is likely an atmospheric response of the amorphous Ca, Ga, and O species. At approximately 650 °C the unknown phase(s) disappear(s) and a multiphase mixture forms with peaks suggesting a compound isostructural to the $\text{Ca}_{12}\text{Al}_{14}\text{O}_{33}$, with Ga substituted

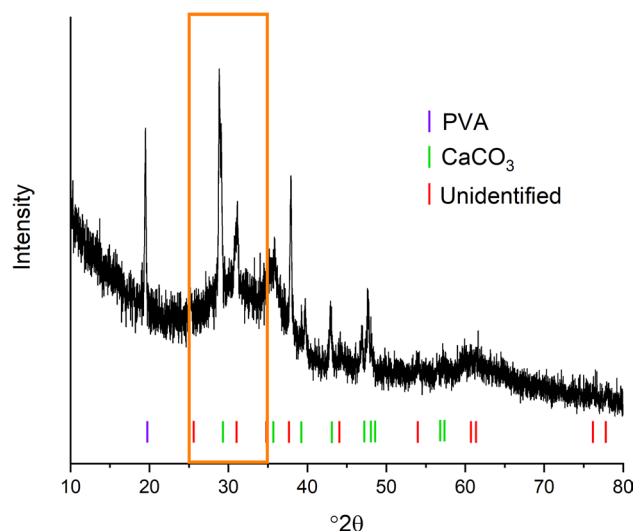


Figure 4. Larger data collection range collected at 500 °C. The region in the box corresponds to the region collected during the fast data collection (Fig. 3b). Data collected on PVA and peak markers for CaCO_3 are included for comparison. Dash marks for indicating the PVA and CaCO_3 phases determined from the ICSD¹⁷ and ICDD²⁸ databases.

on the Al sites, along with CaGa_4O_7 (ICSD 10351) as a minor secondary phase (Fig. 3c). The peaks belonging to the $\text{Ca}_{12}\text{Ga}_{14}\text{O}_{33}$ compound get sharper and more intense as the temperature increases, consistent with phase and crystallite growth. CaGa_4O_7 is present between 650 and 750 °C disappearing above 750 °C. The presence of this Ga rich phase could indicate a non-equilibrium assemblage that forms due to the high heating rate or potentially during the solution-based synthesis where nonstoichiometric areas of the precursor form but get quickly removed when the diffusion increases with higher temperature. Above 750 °C (Fig. 3d) single phase $\text{Ca}_{12}\text{Ga}_{14}\text{O}_{33}$ is present until a new peak at approximately $31.5^\circ 2\theta$ appears at 975 °C (Fig. 3e). To identify the additional phase that is represented by the new peak, data were collected on a larger $^\circ 2\theta$ range (10– $80^\circ 2\theta$) at 1000 °C. It was confirmed that the peak belongs to the CaO and using the Rietveld technique results in 19.8(3) wt% of CaO with all peaks in the pattern accounted for by either $\text{Ca}_{12}\text{Ga}_{14}\text{O}_{33}$ or CaO.

A pellet of the amorphous sol–gel reactants was fired at 800 °C to form $\text{Ca}_{12}\text{Ga}_{14}\text{O}_{33}$ and high spatial resolution X-ray diffraction data were collected on the powdered sample at room temperature to verify the phase purity and characterize the crystal structure. To verify the crystal structure Rietveld refinements using two different models, based on the $\text{Ca}_{12}\text{Al}_{14}\text{O}_{33}$ structure, were attempted. The two slightly different atomic structures were reported by Bartl and Scheller³⁰, determined from single crystal X-ray diffraction data, and Boysen et al.³¹ (ICSD 241000) determined from neutron powder diffraction data. Both structures crystallized in the cubic crystal system, space group $I\bar{4}3d$ (space group number 220) and with a unit cell edge close to 12 Å. The structure by Boysen et al.³¹ differed from the structure by Bartl and Scheller³⁰ by having two unique partially occupied Ca positions on 24d sites as opposed to one fully occupied Ca 24d site. Another difference between the two reported structures is that Bartl and Scheller³⁰ placed the caged O on a 24d site ($x, 0, \frac{1}{4}$, specifically 0.337, 0, $\frac{1}{4}$) with a corresponding site occupancy of 0.083 for filling approximately two of the 12 cages/unit cell. Boysen et al.³¹ working with neutron powder diffraction data, which is more sensitive to the O atoms (the bound coherent neutron scattering lengths for Ca, Al, and O are 4.70, 3.449, and 5.803 fm, respectively³²) moved the caged O from 0.337 to 0.375 or the 12a site ($\frac{3}{8}, 0, \frac{1}{4}$) with a correspondingly higher site occupancy for filling approximately two of the 12 cages/unit cell. Additional studies have been carried out using synchrotron radiation to understand the details of the cage distortions and cage occupancy^{33,34}. The intent of the characterization studies presented here is not to provide crystallographic details but to confirm the isostructural nature of $\text{Ca}_{12}\text{Ga}_{14}\text{O}_{33}$ to $\text{Ca}_{12}\text{Al}_{14}\text{O}_{33}$ and the model that fits best.

When using the structure with the two unique partially occupied Ca sites and caged O on the 12a site³¹ and changing the Al atoms to Ga atoms, it was impossible to refine on the atomic displacement parameter (adp) for the O atom in the cage center without the isotropic atomic displacement parameter (U_{iso}) going negative. If the adps for all three oxygens in the structure were constrained together, a positive U_{iso} was obtained but it was impossible to refine on the site occupancy factor of the caged oxygen and obtain a physically reasonable result. When the site occupancy factor was fixed at $\frac{1}{6}$ and the U_{iso} of the three oxygens constrained together, plausible results were obtained, however, there were intensity mismatches, shown in Fig. 5, for several of the peaks including the (211), (400), (420), and (422). The resulting agreement factor for the refinement is $wR = 18.54\%$ for a goodness of fit (GOF) (wR/wR_{min}) of 1.79. When using the structure with only one Ca position and the caged O on a 24d site³⁰ and changing the Al atoms to Ga atoms it was possible to refine on the adps of the oxygen atoms separately and the site occupancy factor of the caged oxygen. The intensity differences, between the calculated XRD pattern and the observed data, for the reflections discussed above were smaller, as shown in Fig. 6, and a better overall structural model is supported by the resulting smaller $wR = 14.94\%$ and the GOF = 1.44. Upon close

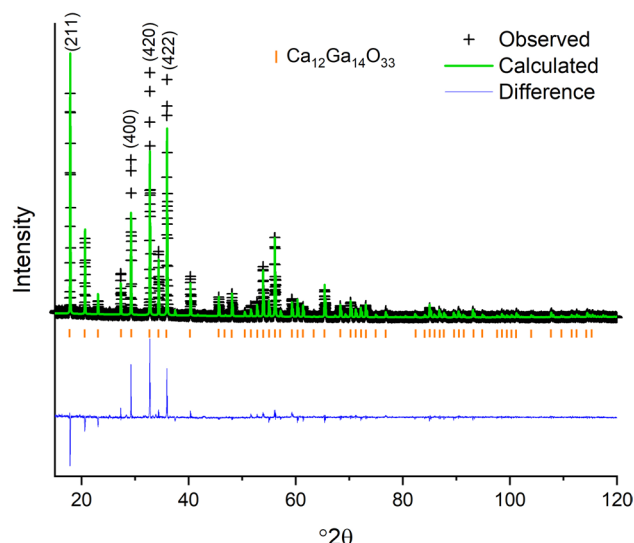


Figure 5. Room temperature XRD data (black crosses), calculated XRD pattern based on the atomic structure with two partially occupied Ca positions and the caged oxygen on the 12a site (green line) and difference pattern (blue line). Graphic generated using the GSAS II software package²⁹, dash marks for indicating the $\text{Ca}_{12}\text{Ga}_{14}\text{O}_{33}$ phase determined from the ICSD¹⁷ and ICDD²⁸ databases.

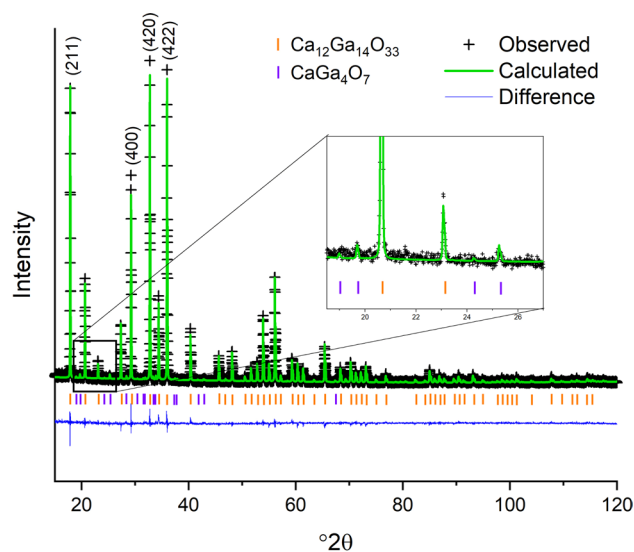


Figure 6. Room temperature XRD data (black crosses), calculated XRD pattern based on the atomic structure with one unique Ca position and the caged oxygen on the 24d site (green line) and difference pattern (blue line). The inset shows a smaller range that contains peaks belonging to CaGa_4O_7 . Graphic generated using the GSAS II software package²⁹, dash marks for indicating the $\text{Ca}_{12}\text{Ga}_{14}\text{O}_{33}$ and CaGa_4O_7 phases determined from the ICSD¹⁷ and ICDD²⁸ databases.

examination there were a few additional weak peaks but these were accounted for by adding a small amount of CaGa_4O_7 ³⁵ as a secondary phase, resulting in a $wR = 13.75\%$ and $\text{GOF} = 1.33$ with 1.9(2) wt% CaGa_4O_7 . Experimental and refinement details, crystal data, and refined fractional coordinates, site occupancy factors, and isotropic thermal parameters are given in Tables 1, 2, and 3, respectively. The above suggests the better structural model for $\text{Ca}_{12}\text{Ga}_{14}\text{O}_{33}$ is the model with only one Ca position and the caged O in the 24d site³⁰. However, given the low occupancy of any atomic or molecular species occluded in the cage, coupled with the occluded species having fewer electrons than the framework elements, Ca and Ga, the best structural model will depend on the elusive occluded atomic or molecular species.

Neutron powder diffraction characterization. Four detector banks of time-of-flight neutron powder diffraction data were collected at room temperature. The data show an elevated background, approximately four times that of the background of the data collected on the Si Standard Reference Material (SRM) (NIST Si 640

	XRD		NPD	
Model	2 Ca	1 Ca	2 Ca	1 Ca
Caged O site	12a	24d	12a	24d
Goodness of fit, GOF	1.79	1.33	16.59	16.61
wR (%)	18.54	13.75	4.83	4.84
Instrument type	Bragg–Brentano		Debye–Scherrer	
Data range	15–120°2θ		0.4–5 d (Å)	
Variables	17	28	59	57
Background	3	3	24	24
Lattice parameter ^a	12.2992(3)	12.2993(3)	12.316(3)	12.316(3)
Sample parameters				
Histogram Scale	1.824(9)	2.093(9)	1/bank	1/bank
Sample displacement (μm)	–472.9(7)	–472.8(6)		
Instrument parameters	1	3	14	14
Atomic positions	7	7	7	7
Adps (U _{iso})	4	6	6	6
Site occupancy factors (caged O)	0	1	1	1
Second phase (CaGa ₄ O ₇) wt%	–	1.92(9)	–	–
Lattice parameters for CaGa ₄ O ₇ , a, b, c, and β	–	4	–	–

Table 1. Experimental information, refinement parameters, and results. ^aLattice parameter estimated standard deviations are reported as 3σ.

Color	White
Crystal system	Cubic
Space group	$I\bar{4}3d(220)$
a (Å)	12.2993(3)
Volume (Å ³)	1860.5(2)
Z	2
Formula/refined formula	Ca ₁₂ Ga ₁₄ O ₃₃ /Ca ₁₂ Ga ₁₄ O _{39.5}
Formula weight/refined (g/mol)	1985.025/2081.019
Calculated density/refined (g/cm ³)	3.54/3.71

Table 2. Crystal data for Ca₁₂Ga₁₄O₃₃.

Atom	Mult/Wy	x	y	z	sof	U _{iso}
X-ray powder diffraction data						
Ca	24d	0	1/4	0.1402(3)	1	0.0234(13)
Ga	16c	0.01796(12)	0.01796(12)	0.01796(12)	1	0.0231(8)
Ga	12b	–1/8	0	1/4	1	0.0239(11)
O	48e	0.1542(5)	–0.0356(6)	0.0661(6)	1	0.029(3)
O	16c	–0.0611(8)	–0.0611(8)	–0.0611(8)	1	0.038(6)
O	24d	0.4(7)	0	1/4	0.625(14)	0.113(13)
Time-of-flight neutron powder diffraction data						
Ca	24d	0	1/4	0.1433(3)	1	0.017(1)
Ga	16c	0.0190(1)	0.0190(1)	0.0190(1)	1	0.0058(5)
Ga	12b	–1/8	0	1/4	1	0.0055(6)
O	48e	0.1559(2)	–0.0288(2)	0.0633(2)	1	0.0142(5)
O	16c	–0.0654(2)	–0.0654(2)	–0.0654(2)	1	0.030(1)
O	24d	0.38(2)	0	1/4	0.610(9)	0.046(3)

Table 3. Refined fractional coordinates, site occupancy factors (sof) and isotropic thermal parameters (U_{iso}).

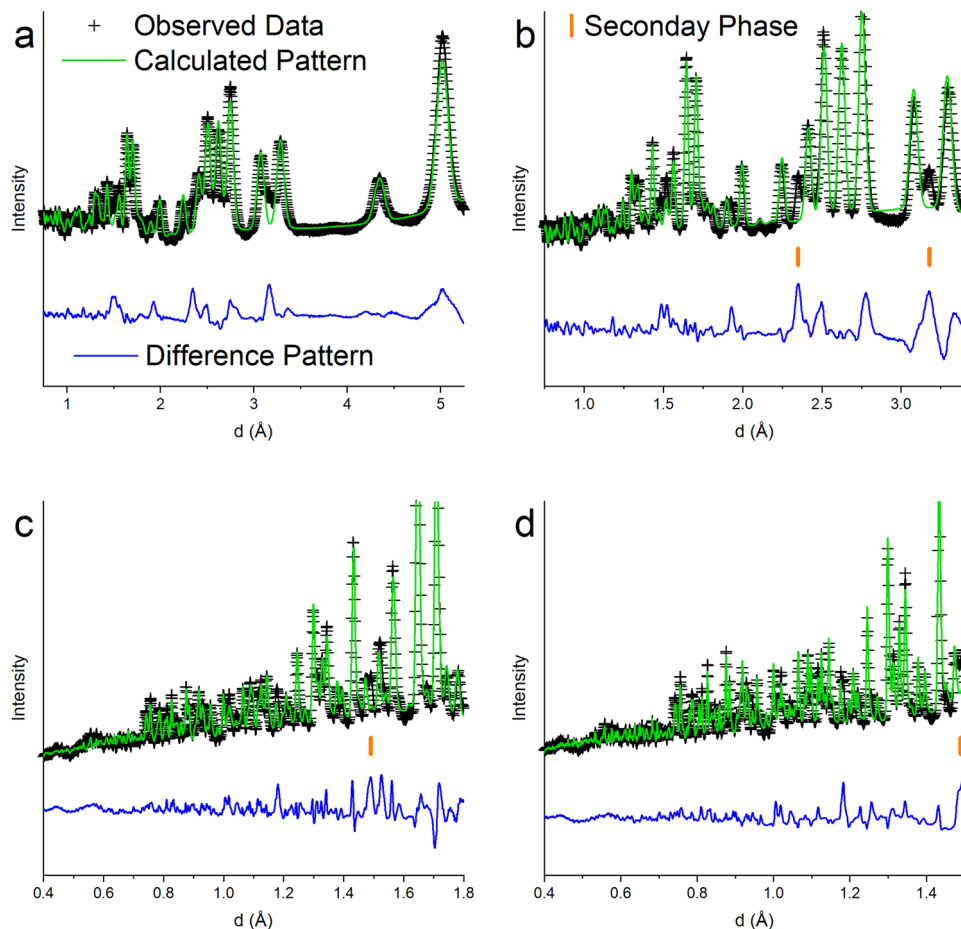


Figure 7. Room temperature time-of-flight neutron powder diffraction data (black crosses) from four detector banks, calculated NPD pattern based on the atomic structure with one unique Ca position and the caged oxygen on the $24d$ site (green line) and difference pattern (blue line). Graphic generated using the GSAS II software package²⁹. Unidentified peaks are marked by the orange dash marks.

E). One reason for the elevated background could be the occupational disorder of the caged O coupled with positional disorder detailed by^{31,32}. Both crystallographic models^{30,31} discussed above were attempted to determine which structural model provided a better fit to the neutron diffraction data. The refinement agreement factors using the model with one Ca position and caged O in the $24d$ site³⁰ were almost identical ($wR=4.84\%$ and $GOF=16.61$ refining on 57 variables) to those obtained using the crystallographic structural model with two unique Ca sites and the caged O on the $12a$ site³¹ ($wR=4.83\%$ and $GOF=16.59$ refining on 59 variables). However, using the model with the two unique Ca positions and the caged O on the $12a$ site when the site occupancy of the caged O was refined it resulted in a value >1 and poor background fitting using the same function and number of coefficients. The refined lattice parameter obtained from the neutron powder diffraction data, $a=12.316(3)$ Å (lattice parameter esds reported as 3σ), is significantly larger than the lattice parameter, $a=12.2993(3)$ Å, refined based on the X-ray diffraction data. Figure 7 compares the calculated patterns, generated from the refined variables, to the observed data in each of the four detector banks. The neutron powder diffraction data show a few unexplained peaks, marked in Fig. 7, at $d=3.17$, 2.35 , and 1.49 Å [the peak at $d=1.49$ Å could be the (300)], suggesting a secondary phase is present. The X-ray diffraction data show secondary phase peaks belonging to CaGa_4O_7 , and this phase was incorporated into the Rietveld analysis and the phase fraction was refined to $1.9(2)$ wt%. The phase diagrams suggest either CaGa_4O_7 , CaGa_2O_4 or $\text{Ca}_3\text{Ga}_4\text{O}_9$ (depending on which phase diagram is correct) should be present in equilibrium, however, none of these compounds have reflections at or near 3.17 and 2.35 Å. Other compounds that were considered included $\text{Ca}_5\text{Ga}_6\text{O}_{14}$, CaO , and CaCO_3 (calcite) but none of these compounds matched the unexplained peaks. Calcite showed the most promise, however, the lattice parameters would need to be shifted far off of the literature values. The search was also opened up to both compounds with the calcite structure but a larger unit cell volume as well as Ca, Ga, O, and H compounds (e.g. $\text{Ca}(\text{OH})_2$, $\text{CaO}_2 \cdot 8\text{H}_2\text{O}$, etc.) but no promising matches were identified. The difficulty in deter-

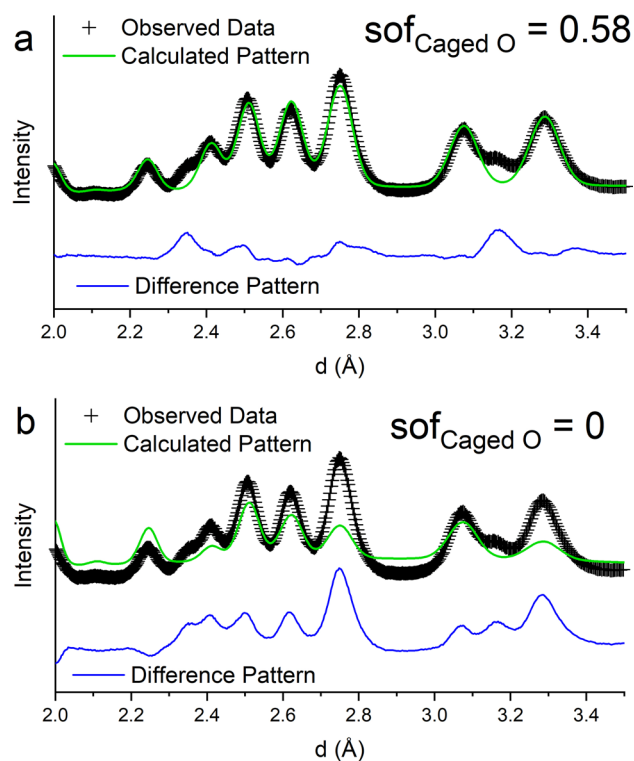


Figure 8. Comparison of the observed data (black crosses) to calculated time-of-flight neutron powder diffraction patterns where the occupancy of the caged O is varied (a) $\text{sof}_{\text{Caged O}} = 0.58$ and (b) cage is empty ($\text{sof} = 0$). Graphic generated using the GSAS II software package²⁹.

mining secondary phases in this study could be due to the ability to definitively determine amount of cage occupant, to charge balance $\frac{1}{6}$ of the cages are occupied by a O^{2-} anion. When using the structural model with one Ca position and the caged O on the $12a$ position³⁰ the site occupancy fraction (sof) of the caged oxygen refined to 0.610(9), only slightly lower than that determined by the X-ray powder diffraction study ($\text{sof} = 0.62(1)$), and still high compared to $\text{sof} = 0.167$ that should result if one out of every six cages are occupied. Figure 8 illustrates how manually changing the site occupancy of the caged oxygen atom has a significant impact on several of the peaks in the neutron powder diffraction pattern. Future work using total scattering or pair distribution function (pdf) analysis on time-of-flight neutron powder diffraction data will reveal more information for a better understanding of the nanoscale structural features of the compound and specifically about the atom(s) present in the $\text{Ca}_{12}\text{Ga}_{14}\text{O}_{33}$ cages. The results presented here are only to provide a second characterization technique that supports the synthesis of $\text{Ca}_{12}\text{Ga}_{14}\text{O}_{33}$.

Comparison of $\text{Ca}_{12}\text{Ga}_{14}\text{O}_{33}$ to $\text{Ca}_{12}\text{Al}_{14}\text{O}_{33}$ and conclusions

$\text{Ca}_{12}\text{Ga}_{14}\text{O}_{33}$ was successfully synthesized using the polymer-assisted steric entrapment method²⁵. X-ray and neutron diffraction data indicate that the new compound is isostructural to $\text{Ca}_{12}\text{Al}_{14}\text{O}_{33}$ with a full exchanged of Al to Ga. HTXRD showed a formation temperature of 650 °C, which is significantly lower than that observed for $\text{Ca}_{12}\text{Al}_{14}\text{O}_{33}$ synthesized in a similar manner⁸. The best refinement, based on both the laboratory XRD and time-of-flight neutron powder diffraction data, resulted with the model that only has one Ca position and the caged O on the $24d$ site. The refined lattice parameter for the new $\text{Ca}_{12}\text{Ga}_{14}\text{O}_{33}$ compound is $a = 12.2993(3)$ Å (XRD), approximately 2.6% larger than the 11.9794 Å of $\text{Ca}_{12}\text{Al}_{14}\text{O}_{33}$ ³¹. This expansion in lattice parameter leads to a 1.6% expansion of the cages as shown in Fig. 9. The larger framework and cages potentially open the possibility of occluding larger molecular species within the cage. Future work is needed to elucidate the current cage occupants, better understand the local structure of the compound, determine potential processing conditions that converts the compound into an electride structure, and evaluate the changes in electrical properties based on cage occupants.

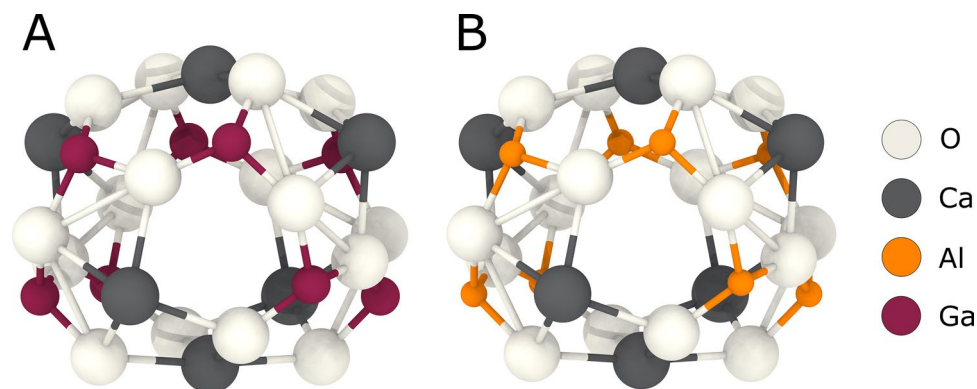


Figure 9. Comparison of $\text{Ca}_{12}\text{Al}_{14}\text{O}_{33}$ (A) and $\text{Ca}_{12}\text{Ga}_{14}\text{O}_{33}$ (B) cages. The distance between the Ca at the top and bottom of the cage, indicated by the dashed line, is 5.642 Å in the $\text{Ca}_{12}\text{Al}_{14}\text{O}_{33}$ cage and 5.734 Å in the $\text{Ca}_{12}\text{Ga}_{14}\text{O}_{33}$ cage. This corresponds to a 1.6% expansion in the cage diameter. Graphic generated using the OVITO software package³⁶.

Received: 8 July 2020; Accepted: 10 September 2020

Published online: 01 October 2020

References

- Lacerda, M., Irvine, J. T. S., Glasser, F. P. & West, A. R. High oxide ion conductivity in $\text{Ca}_{12}\text{Al}_{14}\text{O}_{33}$. *Nature* **332**, 525–526. <https://doi.org/10.1038/332525a0> (1988).
- Li, Z. S., Cai, N. S. & Huang, Y. Y. Effect of preparation temperature on cyclic CO_2 capture and multiple carbonation—calcination cycles for a new Ca-based CO_2 sorbent. *Ind. Eng. Chem. Res.* **45**, 1911–1917. <https://doi.org/10.1021/ie0512111> (2006).
- Li, C. S., Hirabayashi, D. & Suzuki, K. Development of new nickel based catalyst for biomass tar steam reforming producing H_2 -rich syngas. *Fuel Process. Technol.* **90**, 790–796. <https://doi.org/10.1016/j.fuproc.2009.02.007> (2009).
- Trofymuk, O., Toda, Y., Hosono, H. & Navrotsky, A. Energetics of formation and oxidation of microporous calcium aluminates: a new class of electrides and ionic conductors. *Chem. Mater.* **17**, 5574–5579. <https://doi.org/10.1021/cm051662w> (2005).
- Salasin, J. R. & Rawn, C. J. Structure property relationships and cationic doping in $[\text{Ca}_{24}\text{Al}_{28}\text{O}_{64}]^{4+}$ framework: A Review. *Crystals* **7**, 1–25. <https://doi.org/10.3390/cryst7050143> (2017).
- Shannon, R. D. Revised effective ionic radii and systematic studies of interatomic distances in halides and chalcogenides. *Acta Crystallogr. A* **32**, 751–776. <https://doi.org/10.1107/S0567739476001551> (1976).
- Palacios, L., Bruque, S. & Aranda, M. A. G. Structure of gallium-doped mayenite and its reduction behaviour. *Phys. Status Solidi B* **245**, 666–672. <https://doi.org/10.1002/pssb.200743425> (2008).
- Salasin, J. R. & Rawn, C. J. In-situ kinetic investigation of calcium aluminate formation. *Ceramics* **1**, 175–197. <https://doi.org/10.3390/ceramics1010016> (2018).
- Salasin, J. R. *et al.* Direct formation and structural characterization of electride C12A7. *Materials* **12**, 1–22. <https://doi.org/10.3390/ma12010084> (2019).
- Wisnyi, L. G. The High Alumina Phases in the System Lime-Alumina. Ph.D. Dissertation (Rutgers University, New Brunswick, 1955).
- Lea, F. M. & Desch, C. H. *The Chemistry of Cement and Concrete* 2nd edn, 637 (St. Martins Press, New York, 1956).
- Jerebstov, D. A. & Mikhailov, G. G. Phase diagram of the $\text{CaO}-\text{Al}_2\text{O}_3$ system. *Ceram. Int.* **27**, 25–28. [https://doi.org/10.1016/S0272-8842\(00\)00037-7](https://doi.org/10.1016/S0272-8842(00)00037-7) (2001).
- Nurse, R. W., Welch, J. H. & Majumdar, A. J. The $\text{CaO}-\text{Al}_2\text{O}_3$ system in a moisture-free atmosphere. *Trans. Br. Ceram. Soc.* **64**, 409–418 (1965).
- Jeevaratnam, J. & Glasser, F. P. The system $\text{CaO}-\text{Ga}_2\text{O}_3$. *J. Am. Ceram. Soc.* **44**, 563–566. <https://doi.org/10.1111/j.1151-2916.1961.tb11658.x> (1961).
- Young, I. M. The central region of the calcium oxide–gallium oxide system. *J. Mater. Sci.* **14**, 3008–3010 (1979).
- Kovba, L. M., Lykova, L. N. & Kalinina, T. A. *Zh. Neorg. Khim.* **25**, 725–728 (1980) [*Russ. J. Inorg. Chem. (Engl. Transl.)*, **25**, 397–399 (1980)].
- Inorganic Crystal Structure Database (ICSD), FIZ Karlsruhe. <https://icsd.products.fiz-karlsruhe.de/>
- Kahlenberg, V. & Shaw, C. S. J. $\text{Ca}_2\text{Ga}_2\text{O}_5$: a new high pressure oxogallate. *Zh. fur Kristallographie* **216**, 206–209. <https://doi.org/10.1524/zkri.216.4.206.23257> (2001).
- Bilyi, A. I. *et al.* Crystal structure of $\text{Ca}_5\text{Ga}_6\text{O}_{14}$. *Kristallografiya* **31**, 1217–1219 (1986).
- Merinov, B. V., Londar, S. L. & Zakharko, Y. M. Crystal structure of $\text{Ca}_5\text{Ga}_6\text{O}_{14}$ ($5\text{CaO}-\text{Ga}_2\text{O}_3$). *Kristallografiya* **33**, 242–244 (1988).
- Lucco-Borlera, M. & Brisi, C. Composition and structural type of the most basic compound in the $\text{CaO}-\text{Ga}_2\text{O}_3$ system. *J. Less-Common Met.* **125**, L1–L3. [https://doi.org/10.1016/0022-5088\(86\)90102-5](https://doi.org/10.1016/0022-5088(86)90102-5) (1986).
- Londar, S. L. Electroconductivity of $\text{Ca}_5\text{Ga}_6\text{O}_{14}$ crystals. *Phys. Status Solidi (A)* **146**, 765–770. <https://doi.org/10.1002/pssa.2211460221> (1994).
- Tolkacheva, A. S. *et al.* Synthesis, structure, and thermal properties of $\text{Ca}_5\text{Ga}_6\text{O}_{14}$. *Russ. J. Phys. Chem. A* **92**, 1243–1247. <https://doi.org/10.1134/S0036024418070294> (2018).
- Salasin, J. R., Schwertzler, S. E. A., Koehler, M. R., Keffer, D. J. & Rawn, C. J. The effect of process parameters on the amorphous citrate sol-gel synthesis of Cu-doped $\text{Ca}_{12}\text{Al}_{14}\text{O}_{33}$. *Materialia* **4**, 466–477. <https://doi.org/10.1016/j.mtla.2018.11.003> (2018).
- Nguyen, M. H., Lee, S. J. & Kriven, W. M. Synthesis of oxide powders by way of a polymeric steric entrapment precursor route. *J. Mater. Res.* **14**, 3417–3426. <https://doi.org/10.1557/JMR.1999.0462> (1999).
- Neuefeind, J., Feygenson, M., Carruth, J., Hoffmann, R. & Chipley, K. K. The nanoscale ordered materials diffractometer NOMAD at the spallation neutron source SNS. *Nucl. Instrum. Methods Phys. Res. B* **287**, 68–75. <https://doi.org/10.1016/j.nimb.2012.05.037> (2012).
- Degen, T., Sadki, M., Bron, E., König, U. & Nénert, G. The HighScore suite. *Powder Diffr.* **29**(Suppl 2), S13–S18 (2014).

28. Gates-Rector, S. & Blanton, T. The powder diffraction file: a quality materials characterization database. *Powder Diffr.* **34**, 352–360. <https://doi.org/10.1017/S0885715619000812> (2019).
29. Toby, B. H. & Von Dreele, R. B. GSAS-II: the genesis of a modern open-source all purpose crystallography software package. *J. Appl. Crystallogr.* **46**, 544–549. <https://doi.org/10.1107/S0021889813003531> (2013).
30. Bartl, H. & Scheller, T. Zur struktur des $12\text{CaO}\cdot 7\text{Al}_2\text{O}_3$. *Neues Jahrb. fur Mineral.* **35**, 547–552 (1970).
31. Boysen, H., Lerch, M., Stys, A. & Senyshyn, A. Structure and oxygen mobility in mayenite ($\text{Ca}_{12}\text{Al}_{14}\text{O}_{33}$): a high-temperature neutron powder diffraction study. *Acta Crystallogr. B* **63**, 675–682. <https://doi.org/10.1107/S0108768107030005> (2007).
32. Sears, V. F. Neutron scattering lengths and cross sections. *Neutron News* **3**, 26–37 (1992).
33. Palacios, L., Cabeza, A., Bruque, S., Garcia-Granda, S. & Aranda, M. A. G. Structure and electrons in mayenite electrides. *Inorg. Chem.* **47**, 2661–2667. <https://doi.org/10.1021/ic7021193> (2008).
34. Sakakura, T. *et al.* Determination of the local structure of a cage with an oxygen ion in $\text{Ca}_{12}\text{Al}_{14}\text{O}_{33}$. *Acta Crystallogr. B* **67**, 193–204. <https://doi.org/10.1107/S0108768111005179> (2011).
35. Zheng, W. X. *et al.* Crystal field modulation-control, bandgap engineering and shallow/deep traps tailoring-guided design of a color-tunable long-persistent phosphor (Ca, Sr)Ga₄O₇:Mn²⁺, Bi³⁺. *Dalton Trans.* **48**, 253–265. <https://doi.org/10.1039/c8dt03566k> (2019).
36. Stukowski, A. Visualization and analysis of atomistic simulation data with OVITO—the open visualization tool. *Model. Simul. Mater. Sci. Eng.* **18**, 015012. <https://doi.org/10.1088/09650393/18/1/015012> (2010).

Acknowledgements

SEAM was partially supported by funding from the State of Tennessee and Tennessee Higher Education Commission (THEC) through their support of the Center for Materials Processing. XRD characterization was performed at the Joint Institute for Advanced Materials (JIAM) Diffraction Facility, located at the University of Tennessee, Knoxville. A portion of this research used resources at the Spallation Neutron Source, a DOE Office of Science User Facility operated by the Oak Ridge National Laboratory.

Author contributions

S.E.A.M. conceptualized synthesizing $\text{Ca}_{12}\text{Ga}_{14}\text{O}_{33}$ using the wet chemistry technique employed in the research and synthesized the compound, collected the TGA, HTXRD, and ambient temperature XRD data, and prepared the figures. J.R.S. provided technical direction. S.M.E. collected the NPD data. C.J.R. analyzed the XRD and NPD data. S.E.A.M. and C.J.R. wrote the main manuscript text and J.R.S. and S.M.E. contributed to the manuscript text. All authors reviewed the manuscript.

Competing interests

The authors declare no competing interests.

Additional information

Correspondence and requests for materials should be addressed to C.J.R.

Reprints and permissions information is available at www.nature.com/reprints.

Publisher's note Springer Nature remains neutral with regard to jurisdictional claims in published maps and institutional affiliations.



Open Access This article is licensed under a Creative Commons Attribution 4.0 International License, which permits use, sharing, adaptation, distribution and reproduction in any medium or format, as long as you give appropriate credit to the original author(s) and the source, provide a link to the Creative Commons licence, and indicate if changes were made. The images or other third party material in this article are included in the article's Creative Commons licence, unless indicated otherwise in a credit line to the material. If material is not included in the article's Creative Commons licence and your intended use is not permitted by statutory regulation or exceeds the permitted use, you will need to obtain permission directly from the copyright holder. To view a copy of this licence, visit <http://creativecommons.org/licenses/by/4.0/>.

© The Author(s) 2020